JOURNAL OF SYNCHROTRON RADIATION

ISSN 1600-5775

The optical stretcher as a tool for single-particle X-ray imaging and diffraction

Jan-David Nicolas,[a] Johannes Hagemann,[b] Michael Sprung[b] and Tim Salditt[a]*

[a]Georg-August-Universität Göttingen, Institut für Röntgenphysik, Friedrich-Hund-Platz 1, 37077 Göttingen, Germany, and [b]Deutsches Elektronen-Synchrotron, Notkestraße. 85, 22607 Hamburg, Germany. *Correspondence e-mail: tsaldit@gwdg.de

Received 1 February 2018
Accepted 27 April 2018

Edited by I. Schlichting, Max Planck Institute for Medical Research, Germany

Keywords: X-ray diffraction; X-ray phase-contrast imaging; X-ray holography; three-dimensional reconstruction; biological cells.

Supporting information: this article has supporting information at journals.iucr.org/s

For almost half a century, optical tweezers have successfully been used to micromanipulate micrometre and sub-micrometre-sized particles. However, in recent years it has been shown experimentally that, compared with single-beam traps, the use of two opposing and divergent laser beams can be more suitable in studying the elastic properties of biological cells and vesicles. Such a configuration is termed an optical stretcher due to its capability of applying high deforming forces on biological objects such as cells. In this article the experimental capabilities of an optical stretcher as a potential sample delivery system for X-ray diffraction and imaging studies at synchrotrons and X-ray free-electron laser (FEL) facilites are demonstrated. To highlight the potential of the optical stretcher its micromanipulation capabilities have been used to image polymer beads and label biological cells. Even in a non-optimized configuration based on a commercially available optical stretcher system, X-ray holograms could be recorded from different views on a biological cell and the three-dimensional phase of the cell could be reconstructed. The capability of the setup to deform cells at higher laser intensities in combination with, for example, X-ray diffraction studies could furthermore lead to interesting studies that couple structural parameters to elastic properties. By means of high-throughput screening, the optical stretcher could become a useful tool in X-ray studies employing synchrotron radiation, and, at a later stage, femtosecond X-ray pulses delivered by X-ray free-electron lasers.

1. Introduction

X-ray structural analysis at the level of a single particle has become a reality with the advent of highly brilliant synchrotron and X-ray free-electron laser (FEL) radiation (Miao *et al.*, 1999; Gaffney & Chapman, 2007; van der Schot *et al.*, 2015; Mancuso *et al.*, 2013). Following a hundred years of studying matter by X-ray diffraction in terms of macroscopic ensemble averages, we now have intense focused beams at hand to probe an individual object, separately out of an ensemble. This opens up a unique opportunity to address the polydispersity and polymorphism of soft and biological matter, and to study structure in complex hydrated environments without losing information by ensemble averages. Application examples range from colloidal particles, viruses (Ekeberg *et al.*, 2015) and lipid vesicles to bacteria (Seibert *et al.*, 2010) and eukaryotic cells. To circumvent radiation damage, 'diffract before destroy' or 'diffract before damage' strategies have to be implemented. To this end, samples have to be replenished continuously, and a sufficiently high number of copies have to be probed consecutively. Successive exposures, each time on a new non-identical element of a set, are acquired. Analysis of the entire distribution of structural observables then provides substantially more information than the conventional

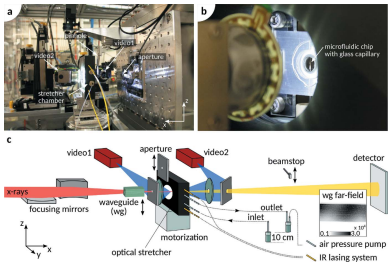

ensemble average, *i.e.* the classical powder and population average. For identical particles, the distribution over which the acquisitions are sampled does not refer to the structure but to the orientation angles. A full dataset for three-dimensional (3D) structure analysis then requires many different views, where each can be sparse in photon counts.

While the potential of single-particle diffraction and imaging in particular on identical particles is undisputed, a tremendous challenge is in realizing suitable sample delivery tools, enabling hydrated environments, precise positioning of the object in the beam, sufficient throughput and hit rate. While liquid jet and droplet technology (aerosol jets) are already quite advanced and have paved the way for studies of smaller, identical particles such as viruses wrapped in a thin hydrated shell (Seibert *et al.*, 2011; Ekeberg *et al.*, 2015), sample delivery of non-identical particles such as larger colloids, bacteria or eukaryotic cells (Kimura *et al.*, 2014; Hantke *et al.*, 2014) require a different approach, both in terms of cross section of the delivery system as well as in view of a need for pre-screening of the object, and eventual rotation and positioning. To this end, channel microfluidics can be made compatible with X-ray experiments using suitable thin foil window materials, as reviewed by Denz *et al.* (2018) and Ghazal *et al.* (2016). As far as trapping, positioning and rotation are concerned, optical forces are the tool of choice to manipulate an individual particle, for example in a channel with or without flow, and to prevent the particle or cell from diffusing out of focus.

For this reason, optical tweezer technology as introduced by Ashkin (Ashkin, 1970, 1978; Ashkin & Dziedzic, 1987) has already received significant attention, and X-ray analysis of trapped particles has been demonstrated for different applications. Examples include diffraction of multilamellar liposomes trapped in an optical tweezer (Cojoc *et al.*, 2007), and starch granules which have even been studied with full control of 3D orientation by Cojoc *et al.* (2010) and also by Santucci *et al.* (2011*a*,*b*). Coherent diffraction imaging (CDI) experiments on particles trapped in an optical tweezer have been reported (Gao *et al.*, 2016). Single-molecule optical trapping and small-angle X-ray scattering studies have been reported by Sivaramakrishnan *et al.* (2009). Finally, X-ray fluorescence measurements of microalgae trapped by optical tweezers have been reported (Vergucht *et al.*, 2015*a*,*b*). The disadvantage of optical tweezers is that the trapping potential is not steep enough to avoid significant motion of the particle. This becomes possible, however, by resorting to the original version of an optical tweezer suggested by Ashkin, which was based on two unfocused counter-propagating laser beams. This configuration, as demonstrated experimentally by Guck *et al.* (2000), can be used to arrest a biological cell at typical laser powers of 100 mW, and even to stress cells for mechanical testing at typical powers of 1 W, excerting forces of the order of 100 pN. In a ray optical picture the surface stress arises by momentum transfer when a laser photon with $p = hn/\lambda$ increases its momentum by entering a medium with higher index of refraction n than its surrounding medium. Alternatively, one can account for the stretching force by calculation of the Maxwell stress tensor (Boyde *et al.*, 2009, 2012). The microfluidic chip design for the dual-beam optical trap and stretcher was first described by Lincoln *et al.* (2007), and more recently the effect of a trapped particle on the beam propagation has been studied by Grosser *et al.* (2015). Apart from cell screening, previous applications of the optical stretcher have also addressed phospholipid assemblies (Delabre *et al.*, 2015) and stretching of giant unilamellar vesicles (GUV) (Solmaz *et al.*, 2012).

In this work, we now demonstrate that the optical stretcher is a well suited tool for single-particle X-ray studies, given its ability to manipulate and rotate a non-adhering biological cell in a flow environment. We show this here for the example of full-field holographic imaging using synchrotron radiation. We first demonstrate the procedure based on polystyrene beads, before we turn to labeled macrophage cells, where we can even show that controlled rotations provide different views for tomographic analysis. Note that in most current studies of cellular imaging, not only by X-rays, cells are imaged while adhering to substrates or are embedded in an extracellular matrix. However, there are also a number of suspension cell types, such as blood cells and many bacteria and other unicellular organisms, where the physiological state of interest is in a suspension. Furthermore, some cases may require the use of fluid flow as an additional control parameter, or even elastic deformation, the application for which the stretcher was devised originally. Note that, based on the technical developments over the last decade, the stretcher has become a screening tool for cell elasticity with statistical throughput rates of about 250 cells per hour. In this work we propose to use this technology for single-cell X-ray studies using high-brilliance synchrotron radiation and FELs. To this end, we take a commercial stretcher with almost no special optimization for the X-ray probe and place it in the nano-focus setup GINIX at the PETRA III storage ring (Salditt *et al.*, 2015). Even without any further optimization (thin foil windows, background reduction) the results already prove the concept.

The article is structured quite simply in the following way. Following this introduction, the experiment is described in §2 along with the associated methods, including the stretcher and the integration into the beamline. §3 then presents the results obtained for polystyrene beads and for macrophage cells, before the article closes in §4 with a brief conclusion and outlook.

2. Experiment

2.1. Optical stretcher system

In the following, we briefly review the essential components of an optical stretcher. For a more in-depth description of the optical stretcher, see Guck *et al.* (2001) and Lincoln *et al.* (2007).

The optical stretcher system (Optical Stretcher, RS Zelltechnik GmbH, Leipzig, Germany) is composed of a microfluidic sample chamber, a laser for cell trapping as well as a height leveling system and an air pressure pump for flow

control. The infrared (IR) laser system can be used to trap or stretch cells in the microfluidic channel. We have used a fiber laser [Fibolux V3.1 (Yb-2x33), FiboTEC, Meiningen, Germany] with an exit wavelength λ of 1060 nm and a maximum continuous wave output power of 1.2 W from two seperate single-mode fibers. The minimum emission power is 50 mW. For the trapping experiment, we have used an output power between 70 and 150 mW per fiber. The two output channels of the laser are fiber-optically coupled to the microfluidic sample chamber where it is integrated into a microfluidic chip. The glass fibers with an exit pupil of approximately 6.5–7 µm are terminated on opposite sites of the glass capillary and positioned such that both glass fibers are co-linear. Only when the glass fibers are well adjusted can cells be efficiently trapped in the capillary. If the output powers from the two fibers are identical, the trap is located in the center between the two fibers. However, detuning the laser power in one fiber results in a shift of the trap location along the beam axis. In this experiment, the output power in both fibers was identical.

The overall design of the microfluidic chip is sketched in Fig. 1(*a*). Note that, in contrast to an optical tweezer system, both laser beams are divergent which reduces radiation damage from the IR laser to a neglible minimum. The setup is also well suited to stretch cells. This can be achieved by significantly increasing the laser power up to approximately 1 W per fiber. The stretching of cells is due to an anisotropic stress profile on the cell contour as sketched in Fig. 1(*b*). This feature has not been used in the described experiment, but will certainly be exploited in future studies. Lastly, one should note that the center of the laser trap, defined by the positioning and alignment of the optical fibers during the assembly of the device, is not coinciding with the center of the glass capillary. Given a parabolic centrosymmetric flow profile in the capillary and a stable off-axis trapping center, a cell that is fixed in the trap will therefore experience a torque, as outlined in Fig. 1(*c*). The torque is directly proportional to the applied pressure and hence can be well adjusted by controlling the flow of the surrounding medium. The possibility of tuning the orientation of the cell in the trap can be beneficially used in, for example, tomographic experiments, as will be described later.

A combined system composed of a height leveling system and an air pressure pump was used to precisely vary the flow inside the glass capillary. The height leveling system is maintaining a 10 cm height offset between the cell suspension reservoir (inlet, placed 10 cm below the outlet) and the outlet of the fluidic channel. The air pressure pump is connected to the cell suspension reservoir and compensates the 10 mbar hydrostatic pressure. It can then be controlled within a range of 0 to 30 mbar with an accuracy of 0.1 mbar.

Before loading a new cell suspension, a syringe (1 ml BD Plastipak with Luer-Lock, centric; Becton Dickinson GmbH, Germany) was used to inject an ethanol solution (95 wt% ethanol in ultrapure water) into the microfluidic channel for disinfection and removal of residual trapped air bubbles. Then, the system was flushed with phosphate-buffered saline (PBS) and the cell suspension was injected. Lastly, the syringe was removed from the inlet tube and the tube was inserted into a vial filled with cell suspension. A magnetic stir bar was added to prevent sedimentation of the cells in suspension. The vial was then tightly sealed and the pressure pump was connected to an inlet of the vial.

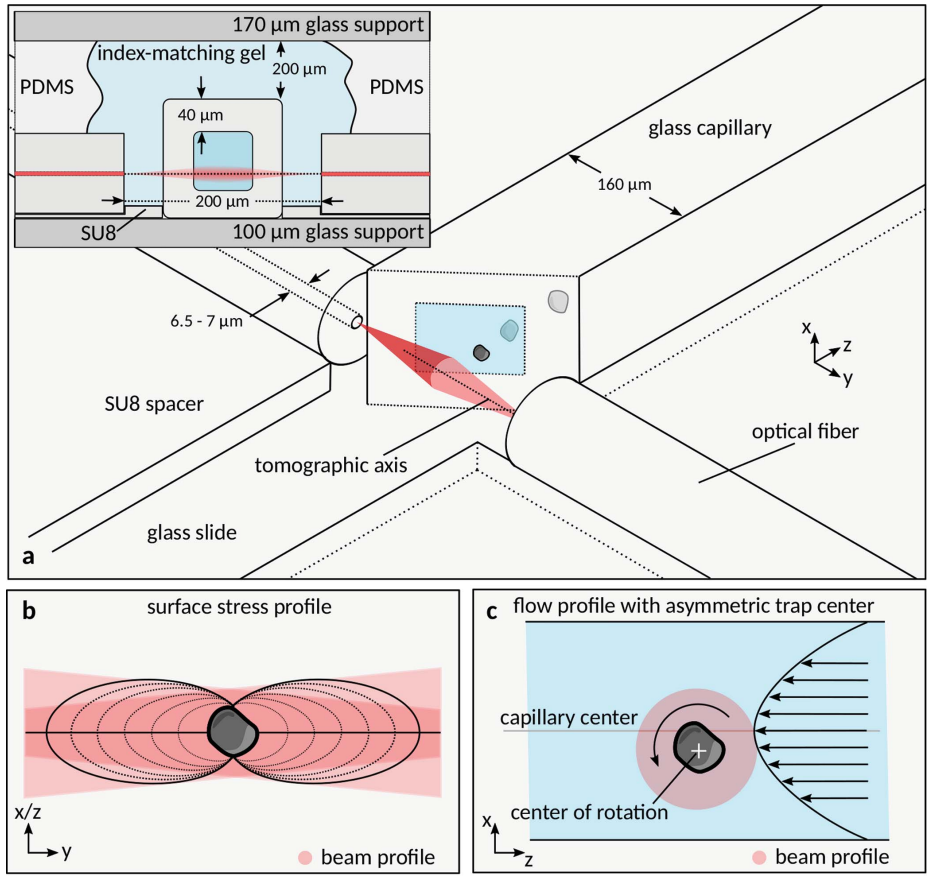

Figure 1
(*a*) Sketch of the integration of the laser system on the microfluidic chip. The capillary is half-cut to give an inside view. Note that the laser beam axis also defines the tomographic axis. The inset shows the central *x*-*y* cross section of the system. Along the propagation direction of the X-ray beam (*x*), the beam transmits through a stack of materials: a supporting glass slide, the capillary glass and the containing fluid, a small layer of index-matching gel for optical microscopy and a covering glass cover slip. (*b*) Highly anisotropic stress profile on the cell contour when a cell is trapped or stretched [adapted from Lincoln *et al.* (2007)]. (*c*) Application of a torque on a trapped cell due to the off-axis positioning of the laser trap.

The optical stretcher system is similar in terms of its operation principle to an optical tweezer. However, at this point one should point out that an optical stretcher offers several technical advantages compared with an optical tweezer. (i) Optical tweezers work at significantly higher flux density for cell trapping. Given an optical tweezer operating at laser powers P_{OT} from 50 mW to 200 mW and with a moderate beam radius ω_0 of around 1 µm, the intensity in the laser focus can be estimated from $I_{OT} = P_{OT}(\pi\omega_0^2)^{-1}$. This yields an intensity ranging between 1500 and 6000 kW cm^{-2}. The optical stretcher described here was operated at approximately 20 kW cm^{-2}, approximated by $I_{OS} = 2P_{OS}\{\pi[d\tan(2\lambda/a_0\pi)]^2\}^{-1}$, where P_{OS} was set to 100 mW per fiber, the distance d between the exit pinhole and the trapping center was 80 µm and the mode field diameter a_0 was 3.1 µm. (ii) Optical stretchers are well suited to trapping large particles such as biological cells since the gradient of the electric field extends over the area of an entire cell, while in an optical tweezer the gradient of the electric field is typically only felt by a small portion of a cell. (iii) The elastic properties of cells can be measured by the stretching capability of the optical stretcher.

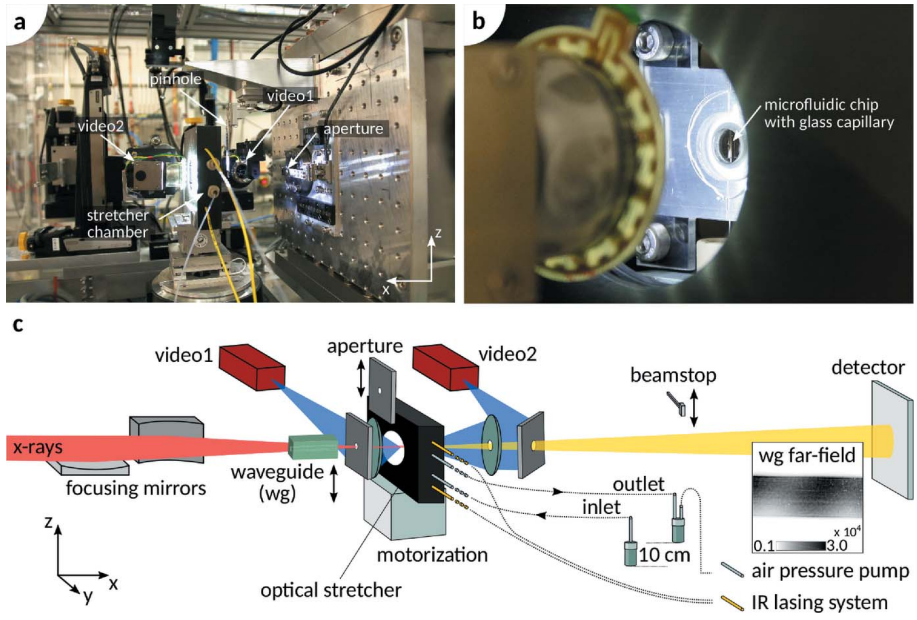

Figure 2
The optical stretcher mounted into the GINIX setup of the P10 endstation at PETRA III, DESY. (*a*) Photograph of the setup during alignment with the X-ray beam. (*b*) Close-up photograph of the interior of the chamber. Upon close inspection, one can observe the 160 µm-thick vertical capillary and the index-matching gel. (*c*) Experimental configuration for X-ray phase-contrast imaging and scanning X-ray diffraction. In the phase-contrast setting, KB focusing mirrors steer the beam into the entrance pupil of a one-dimensional X-ray waveguide (wg). The far-field pattern of the X-ray beam is shown in the inset. For scanning diffraction studies, the stretcher chamber is placed into the focus of the KB beam. A beamstop is inserted to block the primary beam. Note that in both configurations the stretcher chamber is connected to a height leveling system and an air pressure pump for flow control as well as an IR lasing system for optical trapping. For a detailed description of all components depicted in (*c*), see §2.2.

2.2. Integration into the experimental endstation

Data were recorded at the PETRA III endstation P10 (DESY, Germany). For the experiment, the sample chamber was integrated into the GINIX setup (Salditt *et al.*, 2015) which provides the opportunity for both X-ray nano-diffraction and propagation-based X-ray imaging experiments (Nicolas *et al.*, 2017). The X-ray energy was set to 13.8 keV using a Si(111) channel-cut monochromator to achieve a good compromise between phase contrast and a reasonable transmission through a significant amount of glass and liquid.

Due to the compact nature of the optical stretcher, the sample chamber was easily mounted on a motorized sample stage that consists of stepper motors (PI miCos GmbH, Germany) and a piezoelectric stage (SmarAct, Germany) for accurate positioning of the chamber, as depicted in Fig. 2(*a*). The microfluidic chip can be viewed in more detail in Fig. 2(*b*). In this setup, the sample can be viewed with two video cameras that can be inserted before and after the chamber. Both cameras can be used during X-ray exposures, since the beam is transmitted through a hole drilled into the mirror that projects the optical image on the respective CCD.

For phase-contrast imaging experiments (see Fig. 2*c*) we have used Kirkpatrick–Baez (KB) focusing mirrors as a prefocusing device. The beam is hereby steered into the entrance pupil of a one-dimensional X-ray waveguide (wg) for coherence filtering. The optical stretcher is positioned along the propagation axis such that the capillary center is placed 20 mm into the defocus and the hologram is recorded on a scientific CMOS-based detector (pixel size Δx = 6.5 µm; Photonic Science, UK) placed 5.04 m downstream of the focus position. In this configuration, the magnification M is dependent on the position of the sample z_{01} and the detector z_{02} with respect to the focus position of the beam. The magnification is therefore $M = z_{02}/z_{01}$ = 5.046 m/0.02 m = 252.3 and the effective pixel size is $\Delta x_{\rm eff} = \Delta x/M$ = 6.54 µm/252.3 = 25.9 nm. The total photon flux is $I_0 = 7.7 \times 10^9$ photons s^{-1}.

For initial alignment of the chamber, we have removed the waveguide and placed the capillary directly into the focus of the KB beam. In this setting [see Fig. 2(*c*), waveguide moved out of the beam, aperture and beamstop are aligned in the beam], typically used for microfocus and nanofocus diffraction experiments, the focus of the beam is approximately 307 nm × 295 nm in size and the overall photon flux is $I_0 = 9.4 \times 10^{10}$ photons s^{-1}. A movable aperture can be inserted to improve the beam profile several millimetres in front of the sample. To find the intersection between the optical fibers and the glass capillary (see Fig. 3*a*), we have scanned the KB beam

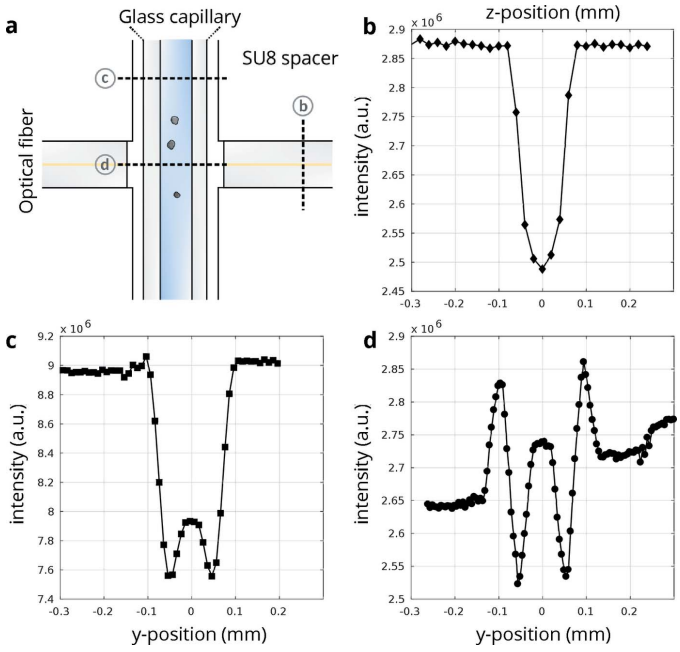

Figure 3
Absorption profiles through the optical fiber, glass capillary and the trap region. (*a*) Sketch of the crossing region between the glass capillary and laser fibers. Black dashed lines are enumerated and correspond to the absorption line profiles in (*b*), (*c*) and (*d*).

vertically along one optical fiber (Fig. 3*b*) and horizontally along the glass capillary (Fig. 3*c*). The scan along the intersection point is shown in Fig. 3(*d*).

Following this initial alignment, we have tested the optical trapping of cells in the capillary. For this, we have used chemically fixed macrophages (MH-S, ATCC CRL-2019; ATCC, USA) with a diameter typically ranging between 10 and 25 µm. The cells could be clearly identified in the capillary as shown in Fig. 4(*a*). Once the trap (here, 100 mW output power per fiber) is activated and a cell is trapped, it is moved into the center of the laser trap. In the optical micrograph, successful trapping can be easily seen by strong scattering of the IR radiation from the cell. Due to photon conversion in the CCD chip, this is clearly visible by a bright violet glow, as depicted in Fig. 4(*b*).

3. Results

3.1. Polystyrene beads

The following experiments have been conducted in the holographic setting as described in §2.2 and depicted in Fig. 2(*c*). As an initial test sample that provides adequate contrast relative to the surrounding medium, we used polymer beads (4210A; Thermo Scientific) with a diameter of 10 ± 0.08 µm and a density of $\rho_{\rm PS} = 1.05\ {\rm g\ cm^{-3}}$ in a solution containing 90 vol% ethanol and 10 vol% ultra-pure water. The maximum phase shift that can be expected is in this case

$$\Delta\varphi = \varphi_{\rm PS} - 0.9\varphi_{\rm ethanol} - 0.1\varphi_{\rm water} = -0.084\ {\rm rad}.$$

For reconstruction of the electron density we have used a phase-retrieval method based on the contrast transfer function (CTF) (Cloetens *et al.*, 1999) which is a single-step procedure as well as an iterative method (using the support of the cell as well as negativity of the phase as constraints) based on the RAAR algorithm (RAAR: relaxed averaged alternating reflections) (Luke, 2005). In Fig. 5(*a*) the original hologram recorded with an exposure time of 0.5 s is shown after division with an empty profile. A black line indicates the central line around which ten lines have been averaged to yield the horizontal line profile shown on the right.

The result of CTF reconstruction is shown in Fig. 5(*b*). Residual low-frequency components could not be removed without further deterioration of the reconstruction quality. Also, horizontal line profiles resulting from horizontal streaks from the KB illumination were amplified in the reconstruction. In contrast to the single-step reconstruction, these artifacts could be minimized using the iterative RAAR algorithm, as shown in Fig. 5(*c*). The RAAR reconstruction was run for 500 iterations. A circle with a radius of 10.6 µm was chosen as support and is indicated by a dashed red line. The corresponding line profile does not yet fit the expected half-circle

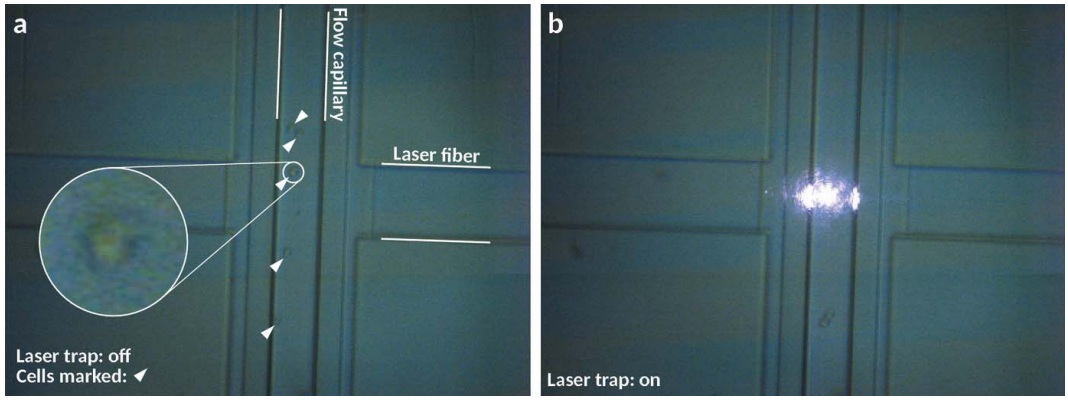

Figure 4
Micrographs of the trapping region obtained using trans-illumination. In (*a*), chemically fixed macrophages are inserted into the microfluidic channel. Single cells are clearly visible in this imaging mode, as can be seen from the inset. (*b*) Upon laser trapping, the cell is pulled into the trap center. Light scattering from the walls of the capillary and from the trapped cell is clearly visible. Here, a trapping power of 100 mW was used.

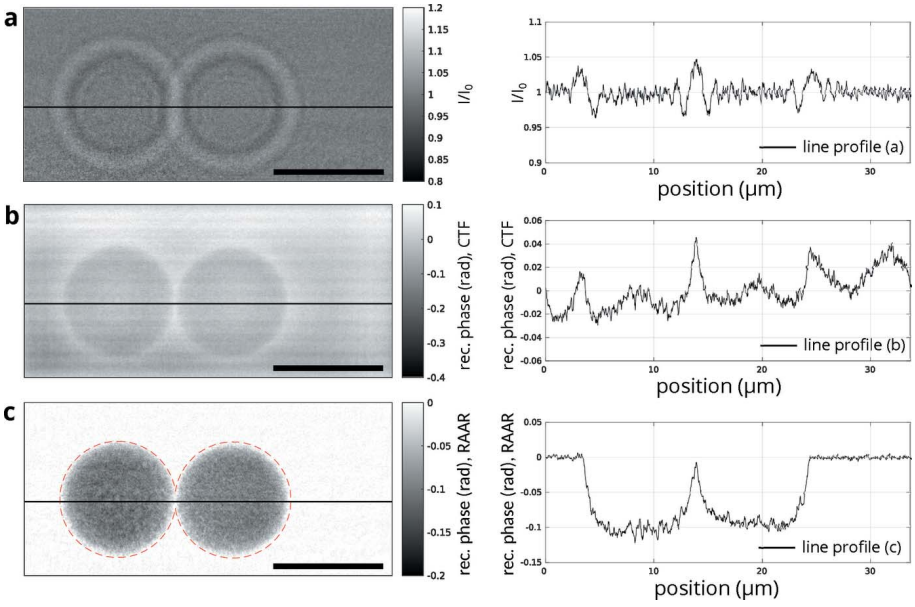

Figure 5
Comparison of reconstruction results from holographic projections of latex beads. (*a*) Hologram of two latex beads in a laser trap. (*b*) Direct reconstruct based on the contrast transfer function. (*c*) RAAR-based iterative reconstruction after 500 iterations. Support is indicated by a red dashed line. Line profiles from the data shown in (*a*)–(*c*) are in each case shown on the right. The line profile was calculated by averaging ten lines around the central line. The position of the central line is indicated on the left by a solid black line. Laser trapping power: 100 mW. Scale bar: 10 μm.

shape. This may be due to the poor recovery of the small spatial frequencies during the holographic reconstruction. Despite this, the corresponding line profiles shown on the right for each image (*a*)–(*c*) confirm that the RAAR reconstruction performs well in reproducing the phase in the interior of the bead.

Taking a movie series of a single polymer bead we observed that during an observation period of approximately 10 s the polymer bead remained accurately trapped with a positional accuracy of $\mathrm{Var}(y) = 310$ nm and $\mathrm{Var}(z) = 404$ nm. The position of the particle was obtained by calculating the center of mass of a thresholded binary image of the reconstructed phase. Based on the equipartition theorem, the variance of the particle movement would translate into a trap stiffness of $k_x = k_\mathrm{B}T\,\mathrm{Var}(x)^{-1} = 1.0 \times 10^{-3}$ pN nm^{-1} and $k_y = k_\mathrm{B}T\,\mathrm{Var}(y)^{-1} = 0.8 \times 10^{-3}$ pN nm^{-1}, given an ambient temperature of 23°C. In addition to a single trapping location, further side minima of the trapping potential along the beam axis might lead to 'hopping' of a trapped particle. The trap stiffnesses reported here are based on a rough estimation of the particle movement. Future applications of the technique will require a more complete characterization of the trap stiffness taking into account, for example, different trapping powers, particle diameters and longer recordings of the particle movement.

3.2. Macrophages loaded with barium sulfate

As a next step, we recorded holograms from chemically fixed macrophages. Since the contrast between suspended single cells and the surrounding medium is very low, we additionally stained the macrophages with barium sulfate, a common contrast agent in computed tomography.

To label the cell culture with barium, we have added 10 μl barium sulfate solution (Micropaque CT, Guerbet, Germany) per 2 ml cell medium. The cell suspension was gently mixed with barium sulfate using a pipette. The solution was then incubated for 4 h at 37°C and 5% CO_2. After incubation, the cells were gently scratched off the surface of the petri dish and centrifuged at 700 r.p.m. for 7 min. The supernatant was then removed and the cells were chemically fixed in a formalin solution (9 wt% formalin in PBS). After a fixation period of several hours, the cells were washed three times in PBS before being used in an experiment.

Barium-labeled macrophage solution was added to the optical stretcher and a single cell was trapped using a trapping power of 100 mW per fiber. A small pressure was applied to the capillary inlet, such that the cell remained trapped but rotated in the capillary. During one rotation, 14 projections were acquired and divided by an empty projection as shown in Fig. 6(*a*). The exposure time for each projection was 0.1 s and the dose per projection shown in Fig. 6 was 927 Gy. Since the dead-time of the detector after each exposure was 1.1 s, an exposure time of 0.1 s corresponds to a cell rotation of 2.1° per projection and one full rotation of the cell took 16.8 s. Each projection was then iteratively reconstructed using 500 iterations of the RAAR algorithm. The reconstructed phase is shown in Fig. 6(*b*). The support has been manually chosen and is indicated as a red dashed line.

Barium sulfate is clearly resolved in the reconstruction. Even the smallest grains of size smaller than 500 nm are clearly visible. The cell contour on the other hand is more difficult to discriminate against the background. Darker regions in the reconstruction seem to depict the cytosol while the contour of the cell is not traceable. It appears that the reconstruction can still recover the cell cytosol even though it is not visible by eye in the projection data.

3.3. Three-dimensional iterative reconstruction of a rotating macrophage

Based on the data shown in Fig. 6, it should in principle be possible to retrieve the phase of the object in three dimensions. Due to a very low number of projections, we have chosen to reconstruct the three-dimensional phase by employing the simultaneous iterative reconstruction technique (SIRT) (Gilbert, 1972). We have used the algorithm as implemented in the *ASTRA* toolbox (van Aarle *et al.*, 2015, 2016).

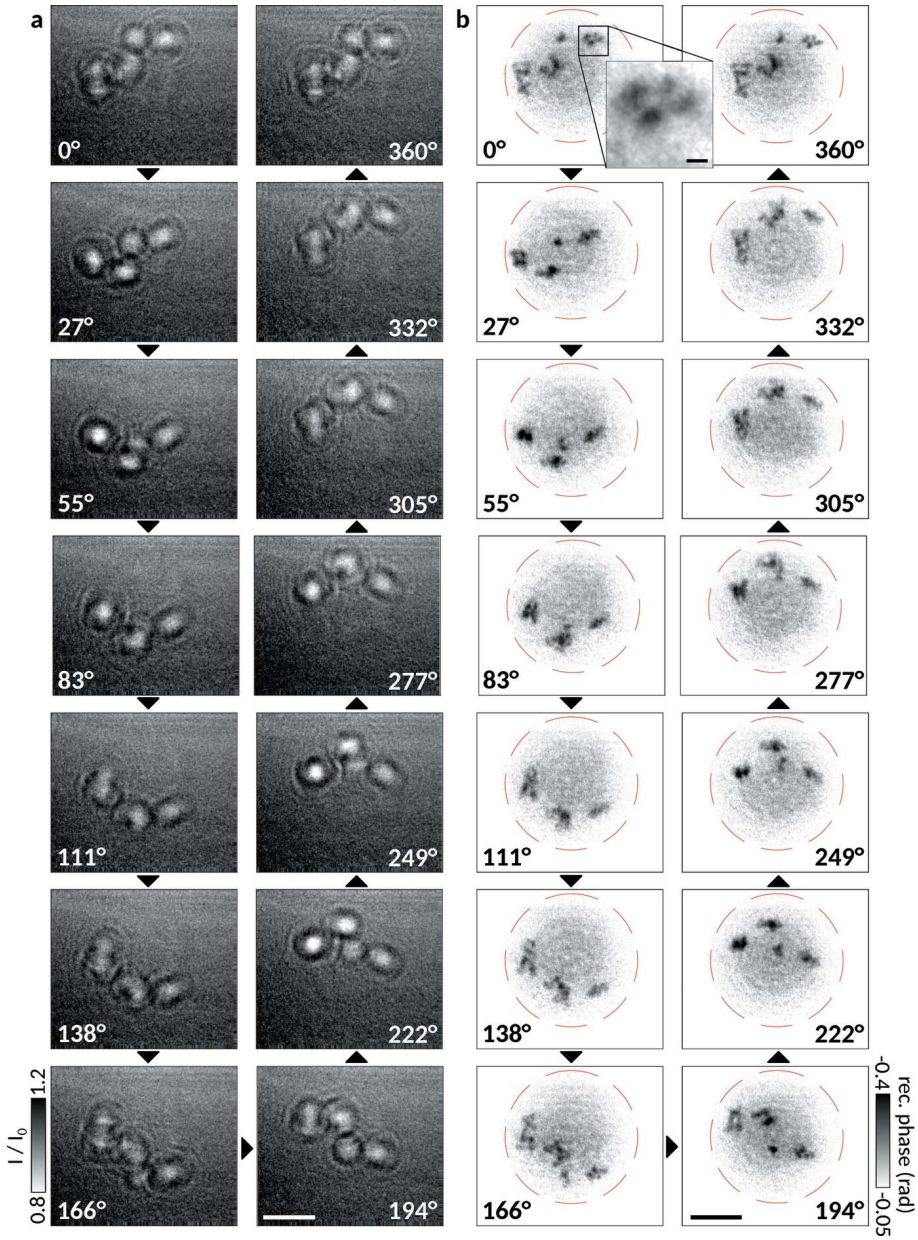

Figure 6
Holographic projections and iterative reconstructions from barium-stained macrophage during rotation in an optical trap. (*a*) Holographic recordings of the rotating cell. Strong fringes appear due to the barium sulfate stain. (*b*) Barium sulfate grains become clearly resolved upon iterative reconstruction. Here, 500 iterations using the RAAR scheme have been used for a good reconstruction. Higher gray values in the center of the cell seem to depict the cell body. The inset shows single barium sulfate particles. Laser trapping power: 100 mW. Scale bar: 5 µm. Scale bar of inset: 500 nm.

For an optimal reconstruction, the data had to be preprocessed prior to the reconstruction. First, to estimate the drift of the cell along the tomographic axis (*y*-axis), the reconstructed phase in Fig. 7(*a*) was thresholded to yield a binary image as shown in Fig. 7(*b*). The center of mass of the three largest connected components of the binary image were calculated and the procedure was repeated for all 14 reconstructions shown in Fig. 6(*b*). This procedure yields the *y*- and *z*-position for each reconstructed frame. The shift along the *y*-axis (Fig. 7*c*) was used to register each frame such that the cell remains horizontally fixed. The *z*-axis of each grain is shown in Fig. 7(*d*) and confirms that one period of rotation is sampled. Secondly, after registering the cell position, the reconstructed data were binned (4 × 4 binning) to reduce artifacts stemming from noise in the reconstruction. Lastly, the set of projections was reconstructed in a parallel beam geometry using the *ASTRA* toolbox and an effective pixel size of 103.7 nm.

To illustrate the final reconstruction result, three views on a volume rendering are shown in Fig. 7(*e*). The volume rendering effect was generated using the Avizo 3D visualization software (*Avizo Lite* 9.2.0, FEI, USA). In orange, the cytosol of the cell is clearly visible. Single barium sulfate grains as seen in the single reconstructions were not retrieved but the barium sulfate aggregations are clearly reproduced and shown in blue. For clarity, markers are added to identify identical barium grains. Due to the limited amount of angles, streak-like artifacts are still visible in the reconstruction.

4. Summary and conclusion

As we have shown, the dual-beam optical trap and stretcher is a promising tool for X-ray imaging of biological cells in the hydrated state by synchrotron radiation and FEL. The holographic reconstructions here were severely limited by the small signal, which in turn required long exposure times. Given the fact that the particles undergo slight movements, the holographic fringes wash out and the small contrast is further diminished. Single FEL exposures unaffected by any motional blurring would therefore provide substantially higher signal, and presumably electron density maps of much higher resolution. At the same time, the background signal of the yet non-optimized microfluidic chip is still substantial and would need to be reduced. With less material to be penetrated, the photon energy could also be lowered which would in turn lead a much stronger contrast.

We also pointed out that, in single-cell experiments, the optical stretcher offers critical advantages compared with an optical tweezer. One key advantage is that, due to the use of a dual beam optical trap with diverent laser beams, cells can be deformed using significantly higher laser powers without

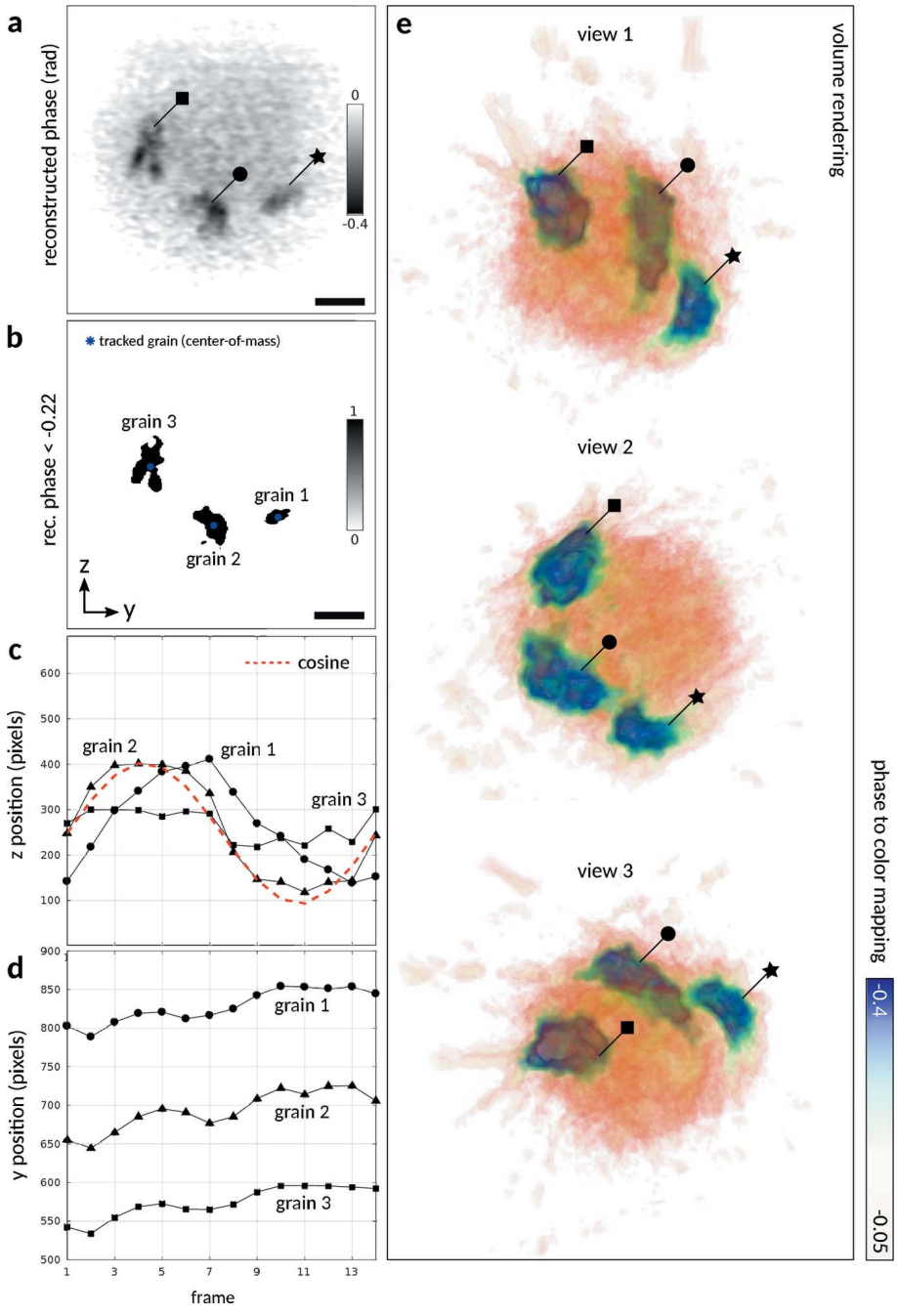

Figure 7
Reconstruction of the barium grains in a three-dimensional volume. (*a*) Iterative reconstruction (low-pass filtered) of a single frame as shown in Fig. 6. (*b*) Binary image using a threshold of −0.22 rad. Black regions indicate phases smaller than the threshold value. The three largest connected components in the binary image are tracked in all frames. (*c*, *d*) Tracked *y*- and *z*-position of the barium grains throughout the scan. Note that all frames are shown in Fig. 6 and used for iterative reconstruction of the three-dimensional volume. (*e*) Volume rendering of the reconstructed 3D phase. Reconstruction was achieved using 50 iterations of the SIRT algorithm implemented in the *ASTRA* toolbox. Prior to reconstruction, the data had been corrected for shifts along the *y*-axis and the rotation axis was placed manually into the center of rotation. Markers are used to indicate identical barium grains. Scale bar: 2.5 µm.

damaging or even opticution of the cell. This brings about the possibility to probe structural changes as a function of the stretching force. By such means, one could, for example, probe stress-induced structural variations of the actin cortex of cells. Joint investigations of structure by X-ray diffraction, and of elasticity using the stretching capability, would also be extremely interesting for studies of vesicles.

The use of a dual-beam optical trap offers the second advantage, that larger particles, in particular suspended cells, can be more easily trapped. We have furthermore shown that, in combination with an X-ray probe, flow control can be very effectively used as a micromanipulation technique that even enables tomographic imaging of cells. This manipulation method, however, has a very low position accuracy and does not work well for particles with an irregular surface. In future experiments, the trapping functionality will therefore be modified such that the sample can be micromanipulated more precisely by optical means.

For all these applications, high throughput and automated analysis is indispensable for conclusive and relevant results, given the polydispersity and polymorphism of the objects studied. While automation relies on the detection of objects in the microfluidic channel, as we saw here, even the modest beamline optical microscope would already provide the required optical control. To this end, it seems that the dual-beam optical trap and microfluidic sample conditioning and delivery is an ideal tool, given the high throughput already demonstrated in its conventional operation without an X-ray probe.

APPENDIX *A*
Rotation of a macrophage

Movie S1 of the supporting information contains a short movie sequences showing the trapping and rotation of a macrophage as viewed in the standard commercial phase-contrast setup. The pump pressure was adjusted such that the cell did not move inside the trap, then the pressure was increased by approximately 100 µbar and the cell started rotating smoothly around its fixation point in the optical trap. Note that the rotation velocity as well as the precise rotation axis is dependent on the shape of the cells. The maximum rotation speed of the cell also critically depends on the trap stiffness. Here, the cell was performing one revolution in approximately 16 s.

APPENDIX *B*
Tracking of macrophages in the microfluidic channel

In movie S2 of the supporting information the outline of the cell was tracked while it was flowing through the capillary channel. In (*a*) the raw data aquired with the on-axis beamline microscrope are shown, while in (*b*) each raw frame was empty subtracted and smoothed. To track the cell, the pre-processed image was thresholded and the center of mass of each connected component in the binary image was tracked (here, a single component is shown). The tracked cell is outlined with a red circle. This demonstrates that the limited capability of the on-axis microscope is sufficient to detect cells in the channel, hence enabling an automatic mode that traps, images and releases cells automatically in a high-throughput fashion.

APPENDIX *C*
Trapping of a macrophage

Movie S3 of the supporting information shows an unstained macrophage that is trapped and released multiple times during the clip duration.

All videos are available as .avi files using Motion JPEG encoding and can be viewed, for example, using the VideoLAN *VLC* software (https://www.videolan.org/vlc/).

Acknowledgements

We thank Dr Markus Osterhoff for continuous developments at GINIX, Bastian Hartmann for engineering support, and Malte Vassholz for support in the alignment of the experimental setup. We are also grateful for the competent advice by the DESY Laser Safety team prior, during and after the experiment. We thank RS Zelltechnik and in particular Roland Stange for providing the instrument and for excellent support as well as helpful discussions.

Funding information

Funding for this research was provided by: Deutsche Forschungsgemeinschaft (grant No. SFB 937, project A11); Bundesministerium für Bildung und Forschung (grant No. O5K16M62).

References

Aarle, W. van, Palenstijn, W. J., Cant, J., Janssens, E., Bleichrodt, F., Dabravolski, A., De Beenhouwer, J., Joost Batenburg, K. & Sijbers, J. (2016). *Opt. Express*, **24**, 25129–25147.

Aarle, W. van, Palenstijn, W. J., De Beenhouwer, J., Altantzis, T., Bals, S., Batenburg, K. J. & Sijbers, J. (2015). *Ultramicroscopy*, **157**, 35–47.

Ashkin, A. (1970). *Phys. Rev. Lett.* **24**, 156–159.

Ashkin, A. (1978). *Phys. Rev. Lett.* **40**, 729–732.

Ashkin, A. & Dziedzic, J. (1987). *Science*, **235**, 1517–1520.

Boyde, L., Chalut, K. J. & Guck, J. (2009). *J. Opt. Soc. Am. A*, **26**, 1814–1826.

Boyde, L., Ekpenyong, A., Whyte, G. & Guck, J. (2012). *Appl. Opt.* **51**, 7934–7944.

Cloetens, P., Ludwig, W., Baruchel, J., Van Dyck, D., Van Landuyt, J., Guigay, J. P. & Schlenker, M. (1999). *Appl. Phys. Lett.* **75**, 2912–2914.

Cojoc, D., Amenitsch, H., Ferrari, E., Santucci, S. C., Sartori, B., Rappolt, M., Marmiroli, B., Burghammer, M. & Riekel, C. (2010). *Appl. Phys. Lett.* **97**, 244101.

Cojoc, D., Ferrari, E., Garbin, V., Di Fabrizio, E., Amenitsch, H., Rappolt, M., Sartori, B., Laggner, P., Burghammer, M. & Riekel, C. (2007). *Appl. Phys. Lett.* **91**, 234107.

Delabre, U., Feld, K., Crespo, E., Whyte, G., Sykes, C., Seifert, U. & Guck, J. (2015). *Soft Matter*, **11**, 6075–6088.

Denz, M., Brehm, G., Hémonnot, C. Y. J., Spears, H., Wittmeier, A., Cassini, C., Saldanha, O., Perego, E., Diaz, A., Burghammer, M. & Köster, S. (2018). *Lab Chip*, **18**, 171–178.

Ekeberg, T., Svenda, M., Abergel, C., Maia, F. R. N. C., Seltzer, V., Claverie, J.-M., Hantke, M., Jönsson, O., Nettelblad, C., van der Schot, G., Liang, M., DePonte, D. P., Barty, A., Seibert, M. M., Iwan, B., Andersson, I., Loh, N. D., Martin, A. V., Chapman, H., Bostedt, C., Bozek, J. D., Ferguson, K. R., Krzywinski, J., Epp, S. W., Rolles, D., Rudenko, A., Hartmann, R., Kimmel, N. & Hajdu, J. (2015). *Phys. Rev. Lett.* **114**, 098102.

Gaffney, K. J. & Chapman, H. N. (2007). *Science*, **316**, 1444–1448.

Gao, Y., Harder, R., Southworth, S., Guest, J., Scherer, N., Yan, Z., Ocola, L., Pelton, M. & Young, L. (2016). *AIP Conf. Proc.* **1741**, 050010.

Ghazal, A., Lafleur, J. P., Mortensen, K., Kutter, J. P., Arleth, L. & Jensen, G. V. (2016). *Lab Chip*, **16**, 4263–4295.

Gilbert, P. (1972). *J. Theor. Biol.* **36**, 105–117.

Grosser, S., Fritsch, A. W., Kiessling, T. R., Stange, R. & Käs, J. A. (2015). *Opt. Express*, **23**, 5221–5235.

Guck, J., Ananthakrishnan, R., Mahmood, H., Moon, T. J., Cunningham, C. C. & Käs, J. (2001). *Biophys. J.* **81**, 767–784.

Guck, J., Ananthakrishnan, R., Moon, T. J., Cunningham, C. C. & Käs, J. (2000). *Phys. Rev. Lett.* **84**, 5451–5454.

Hantke, M. F., Hasse, D., Maia, F. R. N. C., Ekeberg, T., John, K., Svenda, M., Loh, N. D., Martin, A. V., Timneanu, N., Larsson, D. S. D., van der Schot, G., Carlsson, G. H., Ingelman, M., Andreasson, J., Westphal, D., Liang, M., Stellato, F., DePonte, D. P., Hartmann, R., Kimmel, N., Kirian, R. A., Seibert, M. M., Mühlig, K., Schorb, S., Ferguson, K., Bostedt, C., Carron, S., Bozek, J. D., Rolles, D., Rudenko, A., Epp, S., Chapman, H. N., Barty, A., Hajdu, J. & Andersson, I. (2014). *Nat. Photon.* **8**, 943–949.

Kimura, T., Joti, Y., Shibuya, A., Song, C., Kim, S., Tono, K., Yabashi, M., Tamakoshi, M., Moriya, T., Oshima, T., Ishikawa, T., Bessho, Y. & Nishino, Y. (2014). *Nat. Commun.* **5**, 3052.

Lincoln, B., Schinkinger, S., Travis, K., Wottawah, F., Ebert, S., Sauer, F. & Guck, J. (2007). *Biomed. Microdevices*, **9**, 703–710.

Luke, D. R. (2005). *Inverse Probl.* **21**, 37–50.

Mancuso, A. P., Aquila, A., Borchers, G., Giewekemeyer, K. & Reimers, N. (2013). *Scientific Instrument Single Particles, Clusters, and Biomolecules (SPB)*, Technical Design Report DESY-2013–00708, pp. 1–232. DESY, Germany.

Marvin Seibert, M., Boutet, S., Svenda, M., Ekeberg, T., Maia, F. R. N. C., Bogan, M. J., Tîmneanu, N., Barty, A., Hau-Riege, S., Caleman, C., Frank, M., Benner, H., Lee, J. Y., Marchesini, S., Shaevitz, J. W., Fletcher, D. A., Bajt, S., Andersson, I., Chapman, H. N. & Hajdu, J. (2010). *J. Phys. B*, **43**, 194015.

Miao, J., Charalambous, P., Kirz, J. & Sayre, D. (1999). *Nature (London)*, **400**, 342–344.

Nicolas, J.-D., Bernhardt, M., Krenkel, M., Richter, C., Luther, S. & Salditt, T. (2017). *J. Appl. Cryst.* **50**, 612–620.

Salditt, T., Osterhoff, M., Krenkel, M., Wilke, R. N., Priebe, M., Bartels, M., Kalbfleisch, S. & Sprung, M. (2015). *J. Synchrotron Rad.* **22**, 867–878.

Santucci, S. C., Amenitsch, H., Cojoc, D. & Riekel, C. (2011*a*). *Synchrotron Radiation & Structural Proteomics*, edited by E. Pechkova & C. Riekel, Vol. 3 of *Pan Stanford Series on Nanobiotechnology*, ch. 6, pp. 183–211. Pan Stanford Publishing.

Santucci, S. C., Cojoc, D., Amenitsch, H., Marmiroli, B., Sartori, B., Burghammer, M., Schoeder, S., DiCola, E., Reynolds, M. & Riekel, C. (2011*b*). *Anal. Chem.* **83**, 4863–4870.

Schot, G. van der, Svenda, M., Maia, F. R. N. C., Hantke, M., DePonte, D. P., Seibert, M. M., Aquila, A., Schulz, J., Kirian, R., Liang, M., Stellato, F., Iwan, B., Andreasson, J., Timneanu, N., Westphal, D., Almeida, F. N., Odic, D., Hasse, D., Carlsson, G. H., Larsson, D. S. D., Barty, A., Martin, A. V., Schorb, S., Bostedt, C., Bozek, J. D., Rolles, D., Rudenko, A., Epp, S., Foucar, L., Rudek, B., Hartmann, R., Kimmel, N., Holl, P., Englert, L., Duane Loh, N.-T., Chapman, H. N., Andersson, I., Hajdu, J. & Ekeberg, T. (2015). *Nat. Commun.* **6**, 5704.

Seibert, M. M., Ekeberg, T., Maia, F. R. N. C., Svenda, M., Andreasson, J., Jönsson, O., Odić, D., Iwan, B., Rocker, A., Westphal, D., Hantke, M., DePonte, D. P., Barty, A., Schulz, J., Gumprecht, L., Coppola, N., Aquila, A., Liang, M., White, T. A., Martin, A., Caleman, C., Stern, S., Abergel, C., Seltzer, V., Claverie, J.-M., Bostedt, C., Bozek, J. D., Boutet, S., Miahnahri, A. A., Messerschmidt, M., Krzywinski, J., Williams, G., Hodgson, K. O., Bogan, M. J., Hampton, C. Y., Sierra, R. G., Starodub, D., Andersson, I., Bajt, S., Barthelmess, M., Spence, J. C. H., Fromme, P., Weierstall, U., Kirian, R., Hunter, M., Doak, R. B., Marchesini, S., Hau-Riege, S. P., Frank, M., Shoeman, R. L., Lomb, L., Epp, S. W., Hartmann, R., Rolles, D., Rudenko, A., Schmidt, C., Foucar, L., Kimmel, N., Holl, P., Rudek, B., Erk, B., Hömke, A., Reich, C., Pietschner, D., Weidenspointner, G., Strüder, L., Hauser, G., Gorke, H., Ullrich, J., Schlichting, I., Herrmann, S., Schaller, G., Schopper, F., Soltau, H., Kühnel, K.-U., Andritschke, R., Schröter, C.-D., Krasniqi, F., Bott, M., Schorb, S., Rupp, D., Adolph, M., Gorkhover, T., Hirsemann, H., Potdevin, G., Graafsma, H., Nilsson, B., Chapman, H. N. & Hajdu, J. (2011). *Nature (London)*, **470**, 78–81.

Sivaramakrishnan, S., Sung, J., Ali, M., Doniach, S., Flyvbjerg, H. & Spudich, J. A. (2009). *Biophys. J.* **97**, 2993–2999.

Solmaz, M. E., Biswas, R., Sankhagowit, S., Thompson, J. R., Mejia, C. A., Malmstadt, N. & Povinelli, M. L. (2012). *Biomed. Opt. Express*, **3**, 2419–2427.

Vergucht, E., Brans, T., Beunis, F., Garrevoet, J., Bauters, S., De Rijcke, M., Deruytter, D., Janssen, C., Riekel, C., Burghammer, M. & Vincze, L. (2015*a*). *J. Synchrotron Rad.* **22**, 1096–1105.

Vergucht, E., Brans, T., Beunis, F., Garrevoet, J., De Rijcke, M., Bauters, S., Deruytter, D., Vandegehuchte, M., Van Nieuwenhove, I., Janssen, C., Burghammer, M. & Vincze, L. (2015*b*). *Sci. Rep.* **5**, 9049.